

26 **Abstract**

27 Repairing plasma membrane damage is vital to eukaryotic cell survival. Membrane shedding is
28 thought to be key to this repair process, but a detailed view of how the process occurs is still
29 missing. Here we used electron cryotomography to image the ultrastructural details of plasma
30 membrane wound healing. We found that filopodia-like protrusions are built at damage sites,
31 accompanied by retraction of neighboring filopodia, and that these repurposed protrusions act
32 as scaffolds for membrane shedding. This suggests a new role for filopodia as reservoirs of
33 membrane and actin for plasma membrane damage repair. Damage-induced shedding was
34 dependent on F-actin dynamics and Myo1a, as well as Vps4B, an important component of the
35 ESCRT machinery. Thus we find that damage shedding is more complex than current models of
36 simple vesiculation from flat membrane domains. Rather, we observe structural similarities
37 between damage-mediated shedding and constitutive shedding from enterocytes that argue for
38 conservation of a general membrane shedding mechanism.

39 Main

40 Maintaining the integrity of the plasma membrane is critical for the survival of eukaryotic cells,
41 and cells exhibit a rapid response to plasma membrane injury. Injury may include mechanical
42 damage, chemical insults or the introduction of foreign pore-forming proteins such as the
43 bacterial toxin streptolysin O (SLO) or the perforin secreted by cytotoxic T lymphocytes and
44 natural killer cells¹⁻³. Laser ablation of the plasma membrane elicits similar responses².
45 Following damage, a rapid influx of Ca²⁺ and ensuing exocytosis of lysosomes occurs⁴⁻⁶ and the
46 membrane is resealed within a few seconds to a few minutes. Several models, not mutually
47 exclusive, have been proposed for how resealing occurs: (1) in what is known as the “patch
48 model”, a damaged region is replaced by fusion of an intracellular vesicle with the plasma
49 membrane, sloughing off the damaged membrane in the process⁷; (2) in the endocytic model,
50 damaged regions are internalized by endocytosis^{3, 8}; and (3) in the shedding model, damaged
51 regions bud from the plasma membrane and are shed as extracellular vesicles². While the patch
52 model has not yet been validated experimentally, evidence exists for both endocytosis and
53 shedding. For example, SLO-induced pores have been shown to be eliminated by both
54 endocytosis⁹ and shedding^{1, 10, 11}. Several pieces of recent evidence suggest that shedding may
55 be the dominant mechanism for plasma membrane resealing. First, repair occurs even at low
56 temperature, a condition that stalls other mechanisms, including endocytosis¹². Second, after
57 SLO treatment, SLO-containing vesicles are released in an annexin-dependent process^{10, 11}.
58 Third, extracellular vesicle-like structures are observed by scanning electron microscopy (SEM)
59 at sites of laser damage². And finally, Endosomal Sorting Complexes Required for Transport
60 (ESCRT), known to be involved in membrane remodeling processes similar to shedding, were
61 found to be important for resealing small holes (<100 nm)².

62

63 Shedding is a ubiquitous process with diverse functions apart from plasma membrane damage
64 repair. Depending on the cell type, shedding may be constitutive, and is amplified by

65 environmental stimuli¹³. Shed vesicles can deliver enzymes to the intestinal lumen for
66 digestion¹⁴ and detoxification of bacterial lipopolysaccharides¹⁵ to control bacterial population¹⁶.
67 Vesicles released by neutrophils and other immune-response cells regulate inflammation¹⁷⁻¹⁹.
68 Vesicles from astrocytes and neurons contain signaling growth factors^{20, 21}. Vesicles of vascular
69 origin play important roles in angiogenesis, metastasis, atherothrombosis and other diseases²²⁻
70 ²⁴. Despite its importance, the molecular mechanism(s) of shedding remains unclear. The
71 process is best understood in the microvilli of gut enterocytes where central actin bundles are
72 connected to the plasma membrane by spoke-like radial densities of the motor protein Myo1a²⁵.
73 Myo1a is important for stabilizing the microvillus, as well as promoting shedding at the distal tip
74 (possibly by propelling membrane over actin bundles²⁶).

75

76 Here we investigated the ultrastructural details of plasma membrane repair in HeLa cells
77 following laser damage. By electron cryotomography (cryoET), we observed that cells relocate
78 actin and membrane to sites of damage to generate F-actin-rich filopodia-like protrusions that
79 act as scaffolds for vesicle shedding. When N-WASp (required for actin nucleation) or Myo1a
80 was disrupted, cells displayed defects in generating protrusions and shedding vesicles, and
81 disruption of Vps4B, an ESCRT AAA ATPase previously shown to be important for wound
82 repair², led to defects in membrane scission, the final step in shedding. These results reveal that
83 shedding in response to plasma membrane damage is strikingly similar to constitutive shedding
84 from microvilli, suggesting a common underlying mechanism.

85

86 **Results**

87 ***Membrane and actin are relocated to sites of damage***

88 We grew HeLa cells expressing CHMP4B-EGFP, an ESCRT-III protein that gets recruited from
89 the cytosol to the sites of plasma membrane injury, on glass and induced damage with a 640
90 nm laser. Compared to other damage methods including detergents, toxins and mechanical
91 disruption, laser treatment offers reproducibility and precise control over the position of damage
92 sites. It also offers the convenience of administering the insult and monitoring the response with
93 the same instrument, in our case a scanning confocal microscope. We adapted a previously
94 published scheme for laser-based (UV wavelength) damage² by introducing a photosensitizer
95 that causes damage by generating reactive oxygen species (ROS) through fluorescence
96 emission²⁷⁻²⁹. Photosensitizers can be used to specifically damage target cellular compartments
97 such as mitochondria³⁰ and lysosomes³¹. For our workflow, we preincubated cells with the
98 plasma membrane-localized photosensitizer disulfonated aluminum phthalocyanine (AIPcS2a).

99

100 We first standardized the parameters for laser damage. We damaged a 3 μm -wide circular area
101 lacking (by bright-field imaging) filopodia on the edge of a cell. We observed that prolonged
102 laser illumination caused numerous blebs – bulging regions of plasma membrane formed by
103 reorganization of cortical F-actin – around the cells (Supplementary Movie 1 – cell 1). We
104 therefore calibrated the laser illumination by reducing the number of pulse cycles (see Materials
105 and Methods) such that blebbing was limited and cells recovered while remaining attached to
106 the glass surface (Fig. 1, Supplementary Movie 1 – cells 2-6). 150 illumination cycles of the
107 laser produced more reproducible results compared to 100. In total, we imaged the response to
108 laser damage in ~50 cells, with the results summarized in Table 1. Consistent with previously
109 published data², we observed that CHMP4B-EGFP went from being diffusely cytosolic to
110 accumulating at damaged sites (in 40/48 cells) at 5-15 minutes post-damage and reproducibly
111 persisted for at least 40 minutes (Fig. 1). This recruitment of CHMP4B-EGFP was specific to

112 damage sites, compared to randomly chosen control regions nearby (Fig. 1 – viii; note that the
113 control regions Sq2 and Sq3 show some decrease in intensity due to relocation of cytosolic
114 protein and/or photobleaching).

115

116 Several bright-field microscopy observations suggested large-scale remodeling of the plasma
117 membrane (Fig. 1a, Supplementary Movie 1 – cells 2-6). First, plasma membrane blebs formed
118 (32/48 cells) and were subsequently retracted (almost completely in 13/32 cells). The extent of
119 blebbing and subsequent retraction varied from one cell to another. Second, dynamic ruffled
120 membrane boundaries appeared (Supplementary Movie 1 – cells 5-6). Third, existing filopodia
121 near damage sites were retracted (35/48). And fourth, new plasma membrane protrusions were
122 formed at the sites of damage (26/48). These protrusions largely resembled filopodia but
123 sometimes displayed pearling, a phenomenon by which tubular membranes spontaneously
124 stabilize into structures with regularly spaced constrictions, resembling beads on a string^{32, 33}
125 (Supplementary Fig. 1). Numerous new protrusions were observed, beginning 10-15 minutes
126 post-damage, and they continued to appear/persist as CHMP4B-EGFP was recruited. The
127 newly formed protrusions often showed punctate CHMP4B-EGFP fluorescence along their
128 lengths (Supplementary Movie 1 – cell 4). The disappearance of existing filopodia and the
129 appearance of new protrusions were sometimes simultaneous and sometimes sequential. Very
130 few control sites in undamaged cells displayed these phenomena (Table 1). Note that we could
131 not quantify the number of protrusions due to the limited resolution of bright-field imaging, so the
132 appearance of (any) new protrusions in control cells likely reflects random rearrangement of a
133 few filopodia. Indeed, the protrusions formed at damage sites qualitatively outnumber the ones
134 at control sites. Finally, a few damaged cells retracted a portion of their area (6/48; Table 1),
135 forming retraction fibers labeled by CHMP4B-EGFP (Supplementary Fig. 2).

136

137 Phenomena such as blebbing, plasma membrane ruffling and modulation of cell protrusions are
138 suggestive of a role for F-actin. We therefore imaged damage response in cells labeled with
139 RFP-LifeAct. We indeed observed relocation of F-actin to damage sites (Fig. 1, Supplementary
140 Movie 1 – cells 2-3, and quantified in Fig. 1 – ix). Initially, F-actin was enriched in blebs,
141 consistent with its established role in membrane blebbing³⁴. Subsequently, F-actin relocated to
142 the newly formed protrusions.

143

144 ***CryoET reveals F-actin-rich membrane protrusions and free vesicles at damage sites***

145 To study the ultrastructural details of plasma membrane repair, we used electron
146 cryotomography (cryoET), an imaging technique that can provide high-resolution three-
147 dimensional structural information about biological samples preserved in a near-native frozen-
148 hydrated state. Fortunately, the periphery of adherent HeLa cells is thin enough for direct
149 imaging by cryoET. To target damage sites precisely for cryoET, we used CHMP4B-EGFP
150 recruitment as a marker for cryogenic correlative light and electron microscopy (cryo-CLEM). By
151 light microscopy, we observed that cells grown on EM grids were more susceptible to damage
152 and we therefore reduced the damage area to 1.5 μm in diameter and reduced the number of
153 laser pulse cycles to 35. Also, to standardize the recovery time after damage and prevent cells
154 from undergoing large morphological changes between light microscopy and plunge-freezing,
155 we fixed the cells after damage and recovery, before plunge-freezing. Fixation has been shown
156 to largely preserve ultrastructure³⁵⁻³⁷. As with cells on glass, laser-damaging cells on EM grids
157 resulted in CHMP4B-EGFP recruitment at the damage sites by 10-15 min (Fig. 2a). Based on
158 our earlier results, this time point was also ideal to image new cell protrusions at damage sites.
159 We therefore fixed cells between 10 and 15 minutes post-damage (note that the time window
160 was to accommodate multiple photo-damage experiments on each EM grid). The same damage
161 sites were then precisely located by CLEM before imaging by cryoET. This workflow is
162 summarized in Supplementary Fig. 3, and comprehensively shown through a representative

163 experiment in Supplementary Movie 2. We advise readers to watch this movie before
164 proceeding further.

165

166 CryoET of damage sites revealed numerous F-actin-rich plasma membrane protrusions with
167 budding vesicles, and abundant free vesicles nearby (Fig. 2b-d and Supplementary Movie 2).
168 Budding profiles were even observed on the free vesicles. The size distribution of budding
169 profiles matched that of the free vesicles (Fig. 2e; diameter of 85 ± 83 nm for free vesicles and
170 110 ± 92 nm for budding profiles; mean \pm standard deviation (s.d.)), suggesting that the free
171 vesicles were shed from the protrusions. Further supporting this idea, the budding profiles
172 showed protein densities just inside the plasma membrane similar to those present in the shed
173 vesicles. Free vesicles and budding profiles were found on/near filopodia of control cells as well
174 but were relatively rare (Fig. 2d). A subset of damage site protrusions showed regions devoid of
175 F-actin or with disorganized F-actin, usually at their distal tips (Fig. 2c). Such regions had often
176 lost their tubular morphology and displayed a propensity to pearl, consistent with our light
177 microscopy experiments (note that the pearled regions observed by bright-field microscopy
178 were an order of magnitude larger in size). By comparison, filopodia without damage showed no
179 pearling. Pearled membrane protrusions were pleomorphic, with varying numbers of constriction
180 sites. Free vesicles of comparable sizes were abundant in the vicinity (Fig. 2c), suggesting that
181 pearling-mediated membrane constriction contributes to vesicle shedding.

182

183 Damage-induced protrusions resembled canonical filopodia, exhibiting a central bundle of
184 longitudinal F-actin filaments sheathed by plasma membrane (Fig 3a,b). Although the F-actin
185 bundles spanned the entire length of both structures, individual actin filaments were shorter and
186 several filaments were seen originating within the protrusions (consistent with previously
187 characterized filopodia in *Dictyostelium*³⁸). Protrusions at damage sites were as abundant as, or
188 in several cases more abundant than, filopodia seen around control cells (Fig. 3c; note that

189 regular filopodia were non-uniformly distributed, so abundance was measured in clusters).
190 Filopodia and damage site protrusions displayed several other striking similarities: (1) similar
191 widths (Fig. 3d); (2) presence of internal vesicles (Fig. 3e), suggesting active membrane
192 trafficking; (3) linker-like densities between filaments and between F-actin and the plasma
193 membrane (Fig. 3a,b – panels ii-iii); (4) branch points, with F-actin bundles at the periphery (Fig.
194 3a,b – panels iii-iv); (5) F-actin filaments derived from the cortical actin network at the base (Fig.
195 3a,b – panel iv); (6) similar lengths for linear F-actin filaments (Fig. 3f; 122 nm for filopodia and
196 163 nm for damage site protrusions); and (7) lateral inter-filament spacing of ~ 10 nm (10.2 ± 1.3
197 nm for filopodia and 10.1 ± 1.2 nm for damage site protrusions; mean \pm s.d.). By light
198 microscopy, we also observed recruitment of FusionRed fused to Fimbrin/Plastin-1 (Pls1), an
199 actin-bundling protein found in filopodia, into damage site protrusions (Fig. 3g and
200 Supplementary Movie 3). These results, together with the correlation between the appearance
201 of damage site protrusions and the retraction of neighboring existing filopodia, suggest that the
202 protrusions are repurposed filopodia.

203

204 ***Actin-rich membrane protrusions are the source of shed vesicles***

205 The abundance of free vesicles and intermediates around damage-induced protrusions strongly
206 suggests that the protrusions act as scaffolds for shedding. In order to test this hypothesis, we
207 analyzed the damage response in cells after disrupting the N-WASp actin-nucleation pathway
208 with wiskostatin. Wiskostatin binds the GTP-binding domain of N-WASp and stabilizes it in an
209 autoinhibited form³⁹, thus preventing de novo nucleation of linear chains of F-actin or activation
210 of Arp2/3 to form branched F-actin chains. When cells were treated with wiskostatin for 2-3
211 hours, before laser treatment, the number of filopodia visible by bright-field imaging was greatly
212 reduced (Fig. 4a – panels I, iii, and v), although the cells still spread on the glass support. We
213 observed an enrichment of vacuole-like vesicles in these cells, consistent with previous
214 observations⁴⁰, but their significance is unknown. Following laser damage, CHMP4B-EGFP was

215 recruited to the damage site as in untreated cells (Fig. 4a – panels ii, iv, and vi). However, no
216 protrusions were visible by bright-field imaging. CryoET similarly showed a significant reduction
217 in the number of damage site-protrusions compared to untreated cells (Fig. 4b,c). Instead, we
218 observed aberrant membrane structures (not found in untreated cells) that may represent
219 accumulation of membranes that failed to form protrusions (Fig. 4b). Shed vesicles were also
220 less abundant than from untreated cells (Fig. 4d,e). Examination of the vesicles revealed that
221 those from wiskostatin-treated cells showed a narrower range of sizes than those from
222 untreated cells, with fewer vesicles larger than 100 nm in diameter (Fig. 4e). This reduction is
223 reflected in their size distribution (Fig 4d) and their mean sizes (57 ± 44 nm for wiskostatin-
224 treated cells compared to 85 ± 83 nm for untreated cells; mean \pm s.d.). In summary, when actin
225 nucleation is blocked, fewer protrusions and vesicles are observed at damage sites, although
226 CHMP4B-EGFP is still recruited.

227

228 ***Myo1a is involved in the organization of protrusions and/or vesicle shedding***

229 Actin-based membrane protrusions have been previously implicated in vesicle shedding in the
230 brush borders of gut enterocytes^{26, 41}, suggesting possible similarities in the molecular
231 machinery between the two systems. In microvilli, Myo1a forms radial densities connecting actin
232 bundles to the plasma membrane²⁶. We observed similar densities in both filopodia and damage
233 site protrusions (Fig. 3), although they were less abundant, more irregular and harder to quantify
234 than those described in microvilli. We therefore decided to directly test whether Myo1a plays a
235 role in damage-mediated shedding. We knocked down Myo1a expression in cells using siRNAs
236 and observed a significant, though not complete, reduction of Myo1a protein levels
237 (Supplementary Fig. 4a). We then performed damage experiments on cells that showed efficient
238 co-transfection of BLOCK-iT Alexa Fluor Red Fluorescent control RNA (to limit our analysis to
239 transfected cells; Supplementary Fig. 4b). When these cells were laser-damaged, we observed
240 CHMP4B-EGFP recruitment to the damage sites, with or without membrane blebbing, and loss

241 of nearby filopodia and formation of new protrusions (Fig. 5a), just as in wildtype. By cryoET, we
242 observed additional similarities with wildtype: (1) similar abundance of plasma membrane
243 protrusions (Supplementary Fig. 5a); (2) similar organization of F-actin in protrusions (Fig. 5b);
244 (3) pearling at sites of disorganized F-actin along protrusions (Fig. 5b); (4) similar abundance of
245 shed vesicles with comparable size distribution (Supplementary Fig. 5b,c); and (5) protein
246 densities underneath the plasma membrane in both budding profiles and free vesicles (Fig. 5b).
247 These observations indicate that Myo1a is not absolutely essential for the organization of
248 plasma membrane protrusions, although it is also possible that the knockdown of the protein
249 was insufficient to see an effect or that there is significant functional redundancy with other
250 motor proteins. We did, however, observe some defects in scission of budding vesicles (Fig. 5b
251 – panel vi), as well as extended constrictions in protrusions (Fig. 5b – panels vii-viii) that are
252 either disorganized membrane protrusions or defective membrane scission events. Such
253 defects, absent in wildtype, were reflected in the wider distribution of widths for damage site
254 protrusions (Fig. 5c; s.d. of 98 nm for Myo1a knockdown cells and 50 nm for wildtype) and a
255 significant increase in budding profiles (and constriction events) of all sizes compared to
256 wildtype (Fig 5d and Supplementary Fig. 5d). Therefore, Myo1a, although probably not
257 essential, is likely involved in damage-induced shedding.

258

259 ***ESCRT is involved in membrane scission during shedding***

260 ESCRT proteins are known to catalyze several membrane scission processes with similar
261 membrane topology to shedding^{42, 43}. In a previous study, recruitment of ESCRT proteins was
262 shown to directly correlate with wound closure². Furthermore, the authors observed a few
263 extracellular membrane vesicles at sites of damage by SEM, leading to the hypothesis that
264 ESCRT proteins close wounds by shedding damaged membranes. In this study, we observed
265 punctate localization of CHMP4B-EGFP along membrane protrusions at damage sites. These
266 protein foci could be localized to the necks of budding profiles, thus suggesting a role for

267 ESCRT in membrane scission. However, it is also possible that ESCRT is instead localized to
268 endocytic compartments such as multivesicular bodies (MVBs) and other vesicles in the
269 protrusions. We therefore proceeded to directly test the role of ESCRT in membrane shedding.
270
271 We knocked down Vps4B, an essential AAA ATPase in the ESCRT pathway that was
272 previously shown to be important for wound repair, and performed plasma membrane damage
273 experiments. Knockdown of Vps4B was very efficient (Supplementary Fig. 6a) and only cells
274 showing strong signal from co-transfected BLOCK-iT Alexa Fluor Red Fluorescent control RNA
275 were imaged (Supplementary Fig. 6b). Again, we saw that the plasma membrane exhibited
276 blebbing at the site of damage, existing filopodia were retracted around the damage site, new
277 protrusions were formed at the damage site, and CHMP4B-EGFP was recruited to the damage
278 site (Fig. 6a). CryoET of damage sites showed (1) numerous membrane protrusions, (2) F-actin
279 bundles in protrusions, and (3) pearling (Fig. 6b and Supplementary Fig. 7a), all similar to
280 wildtype. Although the abundance of these damage site protrusions seemed to show a different
281 distribution compared to wildtype (as indicated by the p-value from a Kolmogorov-Smirnov test),
282 the mean was quite similar to that of wildtype cells ($\sim 2.5 \mu\text{m}$ of protrusions per μm^2 of tomogram
283 X-Y cross-sectional area for both samples; Supplementary Fig. 7a). These observations indicate
284 that Vps4B is not essential for the organization of membrane protrusions. However, there was
285 an appreciable decrease in the number of shed vesicles smaller than 200 nm in diameter
286 compared to wildtype (Supplementary Fig 7b), as indicated by the mean vesicle diameter ($141 \pm$
287 141 nm for Vps4B knockdown cells compared to $85 \pm 83 \text{ nm}$ for wildtype; mean \pm s.d.). There
288 was a corresponding increase in the abundance of budding profiles (or constriction events)
289 smaller than 200 nm in diameter (Supplementary Fig. 7c). These smaller budding profiles
290 sometimes formed long chains (Fig. 6b – panel v) reminiscent of failed HIV-1 budding profiles
291 from the plasma membrane upon disruption of Vps4 function⁴⁴. Both budding profiles and
292 smaller shed vesicles displayed protein densities underneath their membrane, as seen in

293 wildtype, and the densities were enriched in the chain of budding profiles (Fig. 6b – panel v). In
294 addition to wildtype-like protrusions, we occasionally observed shed protrusions devoid of F-
295 actin (Fig. 6b – panel vi) and a few nested protrusions with or without F-actin (Fig. 6b – panels
296 vii-ix). These defects, not seen in wildtype, are likely due to accumulation of membrane from
297 unshed vesicles upon disruption of Vps4 function and are quantitatively reflected in the greater
298 spread of protrusion widths (Supplementary Fig. 7d; s.d. of 98 nm for Vps4B knockdown cells
299 compared to 50 nm for wildtype). Vps4B is therefore likely involved in membrane scission in
300 damage-induced shedding, particularly for vesicles smaller than 200 nm in diameter, consistent
301 with its published role in closure of small wounds².

302

303 Discussion

304 Here we used correlated light microscopy and cryoET to explore plasma membrane damage
305 repair in HeLa cells. Our findings lead to a model summarized in Fig. 7: (1) actin and membrane
306 from neighboring regions of the cell are relocated to the site of damage; (2) in a process
307 dependent on F-actin nucleation and Myo1a, relocated membrane and actin are used to
308 construct new filopodia-like protrusions to act as scaffolds for vesicle shedding; and (3) F-actin
309 dynamics, Myo1a and the ESCRT machinery mediate membrane remodeling and scission to
310 shed damaged membrane. Damage-induced plasma membrane shedding is thus more complex
311 than current models depicting simple vesiculation from flat plasma membrane domains^{13, 45}.
312 Interestingly, tufts of microvilli-like plasma membrane protrusions were previously reported in
313 bovine retinal microvascular endothelial (BRME) cells in response to wounding⁵, and filopodia-
314 like protrusions were observed in epithelial cells of *Drosophila* embryos upon wounding and
315 were demonstrated to be important for healing⁴⁶. However, the possible function of these
316 structures in membrane shedding remained unknown until now.

317
318 In this study, we observed shedding from membrane protrusions even 10-15 min post-damage,
319 although wound closure has been reported to occur within a couple minutes of damage. It is
320 therefore possible that wound closure involves other mechanisms before shedding discards
321 membrane patches to complete the repair process. For example, reassembly of the actin cortex
322 or recruitment of annexins to the damage site could maintain a diffusion barrier until these
323 membrane patches are shed. Consistent with this hypothesis, annexin A1 and annexin A6 have
324 been previously reported to be enriched in plasma membrane protrusions and shed vesicles
325 upon permeabilization of HEK 293 cells with the toxin SLO¹¹.

326
327 In the first step of shedding, membrane could be transferred to sites of damage by lateral
328 diffusion or by a more complex process involving endocytosis at the source followed by

329 exocytosis at the sites of damage. We observed numerous internal vesicles near damage sites
330 in the cytosol and inside protrusions, supporting the endocytosis-exocytosis model. Retraction
331 of existing filopodia at nearby sites suggests that they contribute actin and membrane for
332 remodeling of damage sites. To our knowledge, a function for filopodia as a reservoir for
333 membrane and actin during plasma membrane repair has not been suggested previously.

334

335 Damage site protrusions may well be repurposed filopodia. They share several features
336 (summarized in results), and are distinguished mainly by the increased shedding from the
337 former. Strikingly, we found that they even share the molecular marker PIs1 (an actin-bundling
338 protein). Consistent with this model, even canonical filopodia exhibit basal levels of shedding,
339 although this function has not been well studied. Filopodia-like protrusions could offer an
340 advantage over a flat patch of plasma membrane by providing a higher membrane curvature
341 more suitable for shedding. As already noted, shedding from brush-border enterocytes occurs
342 from microvilli, another form of plasma membrane protrusions^{26, 41}. Another study reported
343 shedding from mesenchymal cells in response to progesterone treatment via putative vesicle-
344 budding events on plasma membrane protrusions⁴⁷. Thus, shedding from actin-rich membrane
345 protrusions could be a universal mechanism.

346

347 Damage site filopodia are likely built by F-actin along with Myo1a and other motor proteins. As
348 reported for canonical filopodia³⁸, we found several free ends of F-actin throughout the length of
349 all filopodia (including ones at damage sites), supporting a de novo filament nucleation model
350 that describes filopodia growth through multiple nucleation events along its length. Growing F-
351 actin at the tip could provide the force to propel membrane forward while the polymerized F-
352 actin bundles dictate the shape of the filopodia; for example, in curved filopodia we always saw
353 F-actin filaments/bundles of a similar contour closely associated with their plasma membrane
354 (Fig. 3a – panel v). It remains to be seen how different actin nucleation pathways (Arp2/3 vs.

355 Formins) contribute to the formation of damage site filopodia since they show both branched F-
356 actin at their base (consistent with the role of Arp2/3) and long linear F-actin filaments along
357 their length (consistent with Formins). F-actin growth in filopodia could be accompanied by
358 Myo1a or other motor proteins (including Myo1b and Myo6) moving membranes on these
359 filament-tracks towards the tip; Myo1b was reported to localize to filopodia⁴⁸ and an engineered
360 form of Myo6 was shown to induce formation of filopodia⁴⁹, both in HeLa cells. All three motor
361 proteins have been reported to bind phosphoinositides (PIs), which are enriched in filopodia. In
362 addition to plasma membrane moved along F-actin by myosin motors, cytosolic vesicles
363 trafficked internally along F-actin within the filopodia could be used to meet the membrane
364 demands of a growing filopodium. Such internal vesicles, which we observed in damage site
365 filopodia, could also help sort damaged membrane domains to the sites of shedding.

366
367 The final steps of shedding involve membrane deformation and scission in order to release free
368 vesicles to the exterior. It is worth noting that the free vesicles observed in this study showed a
369 very broad size distribution. This size variation and the presence of budding profiles on damage
370 site filopodia argue against the possibility that these vesicles are exosomes (derived from fusion
371 of MVBs with the plasma membrane); exosomes are smaller (<80 nm in diameter) and more or
372 less uniform in size¹³.

373
374 We postulate two different mechanisms, not mutually exclusive, that could cause deformation of
375 membrane domains for shedding: (1) rapid depolymerization of F-actin could cause
376 unsupported membrane to vesiculate or pearl; and (2) membrane-binding proteins could
377 sense/induce high negative curvature, particularly for smaller vesicles. Several previous reports
378 support our first model: (1) destruction of the F-actin cortex with latrunculin A induces pearling of
379 plasma membrane⁵⁰; (2) actin polymerization, destabilization of the actin cytoskeleton and
380 disruption of actin-membrane interactions induce shedding from neutrophils and platelets⁵¹⁻⁵³;

381 and (3) microvilli of enterocytes that shed vesicles from their tip show a similar lack of tubular
382 morphology at their tips that correlates with a lack of F-actin bundles in these regions^{26, 41}. In
383 support of our second model, we observed protein densities underneath membrane regions of
384 high curvature in budding profiles and smaller vesicles. Several inverse BAR (I-BAR) proteins
385 such as IRSp53 have been reported to have high affinity for PIs (enriched in filopodia) and
386 induce negative curvature during various kinds of cellular morphogenesis including filopodia
387 formation^{54, 55}. Moreover, they are known to couple membrane deformation to actin dynamics,
388 an important feature of shedding in our experiments. Involvement of these BAR-domain proteins
389 would not come as a surprise since one such protein, Angiomotin, is known to function in
390 another process involving negative membrane curvature, namely HIV-1 budding from the host
391 cell⁵⁶.

392
393 Subsequent to membrane deformation, the ESCRT machinery is involved in membrane scission
394 during shedding. Previous work hypothesized this function for ESCRT due to their involvement
395 in wound closure and several other membrane scission processes of similar topology². Here we
396 show direct evidence for this function by showing a defect in membrane scission (accumulated
397 budding profiles and a reduced number of free vesicles <200 nm in diameter) when Vps4B
398 function is disrupted. This defect was not complete, so there is likely functional redundancy in
399 the ESCRT system, perhaps with Vps4A.

400 **Methods**

401 **Cell growth**

402 A HeLa Kyoto cell line stably expressing CHMP4B-EGFP (gift from Dr. Anthony A. Hyman, Max
403 Planck Institute) was grown in a humidified 37 °C incubator with a constant supply of 5% CO₂.
404 Cells were cultured in high glucose (L-Glutamine +) Dulbecco's modified Eagle's medium
405 (DMEM; DML09, Caisson Labs, Smithfield, UT) supplemented with 10% fetal bovine serum
406 (FBS; Cat No – 10437028, ThermoFisher), 1 mM sodium pyruvate (Cat No – 11360070,
407 ThermoFisher), 100 units/mL penicillin and 100 µg/mL streptomycin. The CHMP4B-EGFP
408 plasmid was maintained in these cells using 400 µg/mL G-418 disulfate (Cat No – G64500,
409 Research Products International). For experiments involving confocal microscopy, cells were
410 grown on poly-D-lysine-coated 35 mm coverslip bottom dishes (P35GC-1.5-14-C, MatTek
411 corporation). For experiments further involving CLEM and cryoET, cells were grown on 200
412 mesh gold R2/2 London Finder Quantifoil grids (Quantifoil Micro Tools GmbH, Jena, Germany)
413 added to the bottom of MatTek dishes. Prior to addition of these grids to the MatTek dishes,
414 they were coated with 0.1 mg/mL human fibronectin (Cat No – C-43060, PromoCell) by floating
415 them on fibronectin droplets on parafilm for approx. 15-30 min. Additionally, they were coated
416 with 10 nm Au fiducials to be later used for tomography. Roughly 4 µL of 15 X diluted Au
417 fiducials (Cat No – 15703, Ted Pella) in 0.01% bovine serum albumin (BSA) were dried onto the
418 grids. Cells were grown to a density of approx. two to three per grid-square over a period of one
419 to three days depending on the experiment.

420

421 **Gene silencing, expression of fluorescent proteins and drug treatments**

422 Knockdown experiments for Myo1a and Vps4B were performed in CHMP4B-EGFP expressing
423 HeLa cells using Lipofectamine RNAiMax (Cat No – 13778075, ThermoFisher). Cells were
424 grown on 35mm MatTek dishes or on grids placed at the bottom of these dishes overnight. They
425 were transfected with 50 pmol of siMyo1a (SMARTpool ON-TARGETplus MYO1A siRNA, Cat

426 No – L-008765-01, GE Dharmacon) or with 50 pmol of siVps4B (ON-TARGETplus Human
427 VPS4B siRNA, Cat No – L-013119-00, GE Dharmacon). Transfections were performed for two
428 rounds, each lasting for 24 hours. Cells were co-transfected with BLOCK-iT Alexa Fluor Red
429 Fluorescent Control (Cat No – 14750100, ThermoFisher) to ensure transfection efficiency and to
430 identify transfected cells for photo-damage experiments. Transfection experiments with RFP-
431 LifeAct and FusionRed-Fimbrin/Plastin-1 (Pls1) were conducted similar to other transfections
432 before live cell microscopy. For experiments involving Wiskostatin (Cat No – 4434, Tocris
433 Bioscience), the drug was administered to the cells at 25 μ M for 2-3 hours prior to photo-
434 damage experiments.

435

436 **Confocal microscopy and laser damage**

437 Imaging was performed at the Caltech Biological Imaging Facility on a Zeiss LSM800
438 microscope equipped with a large environmental chamber to maintain the temperature at 37 °C
439 and a smaller insert module that helped maintain both the temperature and a CO₂ level of 5%.
440 Prior to confocal microscopy and laser damage, the photosensitizer Al(III) Phthalocyanine
441 chloride disulfonic acid (AlPcS2a; Cat No – P40632, Frontier Scientific) was added to the cell
442 medium at ~1.3 μ M final concentration. Laser damage experiments were performed within the
443 next 10 min to prevent any large interference from endocytosed photosensitizer. No washes
444 were performed after incubation with the photosensitizer. The cell media also contained 50 mM
445 HEPES (Cat No – 15630080, ThermoFisher) to prevent pH fluctuations during cell transport and
446 handling. Both bright-field and fluorescence imaging were performed using an LD C-
447 Apochromat 40 X water-immersion objective with an NA of 1.1 and images were recorded using
448 Photo Multiplier Tubes (PMTs; for bright-field image) and GaAsP-PMT (for fluorescence). Green
449 fluorescence imaging was performed using a diode laser at 488 nm at ~1.5-2% of its maximum
450 power. Photo-damage was administered using a diode laser at 640 nm operated at 100% of its
451 maximum power. The maximum power for the laser lines was 500 mW at the source but

452 measured to be ~750 μ W at the level of the objective lenses for the 488 nm laser and ~400 μ W
453 for the 640 nm laser. We observed that cells grown on EM grids were more susceptible to laser
454 damage than ones grown on glass. Therefore, we reduced the number of laser pulse cycles and
455 the damaged area for cells on EM grids accordingly. For photo-damaging cells grown on glass,
456 a circular area of 3 μ m diameter was chosen close to the cell periphery and scanned for 100 or
457 150 cycles. For cells on grids, a circular area of 1.5 μ m diameter was scanned for 35 cycles.
458 Damage response and recovery were monitored intermittently (~ every 1-2 min) for up to 1 hour
459 after photo-damage. A scan speed of 7 was used for both photo-damaging and imaging cells.
460 The pixel size for imaging was set at 0.312 μ m (0.156 μ m at a zoom factor of 2) while the image
461 sizes were fixed at 512 x 512 pixels. For CLEM and cryoET experiments, cells were fixed at 10-
462 15 min post-damage for 45 min with 4% paraformaldehyde (PFA; Cat No – RT-15710, Electron
463 Microscopy Sciences) in PBS. Cells were washed 3 times with PBS before plunge-freezing for
464 CLEM and cryoET. While studying damage response in cells transfected with siRNAs,
465 candidate cells were chosen based on cytosolic levels of a co-transfected fluorescent BLOCK-iT
466 RNA.

467

468 **Plunge-freezing**

469 EM grids containing photo-damaged and fixed cells were plunge frozen in a liquid
470 ethane/propane mixture using a Vitrobot Mark IV (FEI, Hillsboro, OR)⁵⁷. The Vitrobot was set to
471 95-100% relative humidity at 37 °C and blotting was done manually from the back side of the
472 grids using Whatman filter paper strips. Plunge-frozen grids were subsequently loaded into
473 Polara EM cartridges (FEI) or Krios autogrid cartidges (ThermoFisher). EM cartridges containing
474 frozen grids were stored in liquid nitrogen and maintained at ≤ -170 °C throughout storage,
475 transfer and cryo-EM imaging.

476

477 **Correlative light and electron microscopy (CLEM) and electron cryotomography (cryoET)**

478 Cells previously photo-damaged and imaged by confocal microscopy were imaged by cryo-EM
479 using either an FEI G2 Polara 300 kV FEG cryo-TEM or a ThermoFisher Krios G3i 300 kV FEG
480 cryo-TEM at the Caltech CryoEM Facility. Both these microscopes were equipped with a 4k x 4k
481 K2 Summit direct detector (Gatan, Inc.) operated in electron counting mode. An energy filter
482 was used to increase the contrast at both medium and higher magnifications with a slit width of
483 50 eV and 20 eV, respectively. Additionally, defocus values of close to negative 100 and
484 negative 8 μm were used to boost the contrast (in the lower spatial resolution range) at the
485 medium and higher magnifications respectively. Magnifications typically used on the Polara
486 were 3,000 X and 22,500 X (in the medium and higher ranges), corresponding to pixel sizes of
487 3.7 nm and 4.8 \AA respectively. On the Krios, 3600 X/4800 X and 26000 X were used in the two
488 magnification ranges that correspond to pixel sizes of 4.2 nm/3.1 nm and 5.38 \AA respectively. A
489 Volta phase plate (VPP) was optionally used on the Krios to further improve contrast at higher
490 magnifications in certain cases. SerialEM software⁵⁸ was used for all imaging.

491
492 Photodamaged cells were located in the electron microscope using the markers on the Finder
493 grids. The markers were clearly visible by transmission light microscopy but only partially
494 identifiable by cryo-EM after freezing. However, a full grid montage at a low magnification of
495 close to 100 X is sufficient to positively identify these markers based on their overall
496 arrangement on the grid. The photo-damaged locations in the cells were located by roughly
497 correlating the light microscopy images with the EM maps based on the shape of the cells or by
498 using the image registration protocol in SerialEM. Cracks, regularly spaced 2 μm holes in the
499 carbon film, ice contamination and other features visible by both light and electron microscopy
500 were sufficient to obtain an accurate enough correlation (< 500 nm precision) for the purpose of
501 tomography. Once the areas of interest were identified and marked, anchor maps were used to
502 revisit these locations and collect tilt-series in an automated fashion. Each tilt-series was
503 collected from negative 60° to positive 60° with an increment of 1° or 2° in an automated fashion

504 using the low dose functions of tracking and focusing. The cumulative dose of each tilt-series
505 ranged between 80 and 150 $e^-/\text{\AA}^2$. Once acquired, tilt-series were binned into 1k x 1k arrays
506 before alignment and reconstruction into 3D tomograms with the IMOD software package⁵⁹ and
507 tomo3D⁶⁰. Tilt series were aligned using 10 nm Au fiducials or patch tracking in IMOD while
508 reconstructions were performed using SIRT in tomo3D. In addition to tilt-series, projection
509 images were saved at other magnifications like 360 X for correlation post-data acquisition.

510

511 For data processing, analysis and generating figures, more precise correlations were performed
512 using custom Python scripts in a semi-automated fashion. Features used as control points here
513 were similar to the ones used for correlation during data acquisition. However, the number of
514 control points used was larger and a robust best-fit method was employed to increase the
515 precision for correlation. Control points that gave the most accurate correlation (based on the
516 overall error in the fit) were selected from the set provided by the user for accurate correlation.
517 Precision for correlation at lower magnifications is particularly important because of the large
518 pixel sizes involved.

519

520 **Segmentation**

521 Segmentations of tomograms were manually performed using Amira (ThermoFisher).
522 Animations of segmented tomograms were created using Amira and Adobe Photoshop CC
523 (Adobe Inc., San Jose, USA). Segmentations were done to the best of our abilities bearing in
524 mind the limitation of the missing wedge of information in cryoET. Distinctions between plasma
525 membrane and shed vesicles were based only on unambiguously segmented data.

526

527 **Quantification**

528 *Live-cell light microscopy:* Cells were observed for ~45 minutes post damage (or without
529 damage). Damage sites showing any newly visible filopodia were counted positive for

530 appearance of new protrusions (these protrusions were much more abundant at damage sites
531 than control sites). Integrated intensities over a square area of pixels were plotted over time for
532 damage sites and two other sites from the same cell as control. Intensity data was extracted
533 from live-cell microscopy movies over these square areas using Fiji (ImageJ) before plotting
534 them in Python 3.5 using Numpy and Matplotlib.

535

536 *Actin:* F-actin was analyzed post-segmentation in Amira using the filament module. Actin
537 filaments that were unambiguously linear (no branching, showing free ends on either side) were
538 used for length measurements. A total of ~450 filaments were measured for filopodia and ~480
539 filaments for damage site protrusions. Inter-filament spacing was measured manually at multiple
540 positions between parallel F-actin filaments using IMOD. A total of ~150 measurements were
541 made for filopodia and ~100 for damage site protrusions.

542

543 *Other measurements from cryoET:* Quantifications were performed on a per-tomogram basis.
544 For each damage site, 1-2 tomograms were randomly selected close to the site of CHMP4B-
545 EGFP recruitment. The following numbers of tomograms were selected for each sample – 14
546 tomograms from wildtype damage sites, 10 from control sites with no damage, 11 from damage
547 sites of wiskostatin-treated cells, 8 from damage sites of Myo1a knockdown cells and 11 from
548 damage sites of Vps4B knockdown cells. All measurements were made using IMOD. Density of
549 protrusions was measured as total lengths of protrusions in a tomogram (in μm) divided by
550 tomogram X-Y cross-sectional area (in μm^2). Widths of plasma membrane protrusions were
551 measured at regular intervals at local maxima, minima and anywhere in between. Density of
552 shed vesicles was measured as number of vesicles per μm^2 cross-sectional per tomogram. The
553 vesicle sizes were measured as cross-sectional diameters. Similar quantifications were done for
554 budding profiles as well. New budding profiles in shed vesicles were included in the analysis.
555 Internal vesicles were measured as number of vesicles per μm length of protrusion per

556 tomogram. All model files were exported as text before plotting using Numpy and Matplotlib
557 libraries in Python 3.5. Kolmogorov-Smirnov tests (KS tests) were performed using the ttest_ind
558 method from the Scipy package. We chose one-tailed t-tests for our statistics because our EM
559 data clearly indicated a one-sided shift in the parameter being measured.

560

561 **Acknowledgements**

562 This work was supported by funding from the NIH (P50 AI150464 awarded to G.J.J.). We thank
563 Dr. Anthony A. Hyman and Dr. Ina Poser for providing the HeLa cell line stably expressing
564 CHMP4B-EGFP. We thank Dr. Andres Collazo and Steven Wilbert for technical assistance with
565 confocal microscopy. We also thank Dr. Songye Chen and Dr. Andrey Malyutin for technical
566 assistance with electron cryomicroscopy. The bulk of the confocal imaging was performed at the
567 Biological Imaging Facility and electron microscopy was performed at the Beckman Institute
568 Resource Center for Transmission Electron Microscopy, both at Caltech.

569 **Figure legends:**

570 **Fig. 1: Live-cell light microscopy of plasma membrane damage sites.**

571 Light microscopy images of HeLa cells grown on glass (i) before, and (ii-vii) at various time
572 points after damage – (left-to-right) bright-field, CHMP4B-EGFP and RFP-LifeAct imaging. (viii &
573 ix) Integration of pixel intensities for CHMP4B-EGFP and RFP-LifeAct over the square regions
574 marked as Sq1, Sq2 and Sq3 in (i) at various time points after damage. Sq1 lies over the
575 damaged area while Sq2 and Sq3 are control sites. The damage area (yellow circle) is 3 μm in
576 diameter and the time points after damage are denoted in minutes:seconds. Scale bars – 10
577 μm .

578

579 **Fig. 2: CryoET of plasma membrane damage sites.**

580 (a) CLEM. (i) Cells expressing CHMP4B-EGFP grown on an EM grid. (ii) Sites of laser damage,
581 each 1.5 μm in diameter. (iii) Sites of laser damage showing CHMP4B-EGFP recruitment. Cells
582 were monitored for 10 min post-damage and fixed for 45 min using 4% PFA. (iv) Overlay of
583 fluorescence on electron micrograph. (b-c) CryoET of damage sites and corresponding
584 segmentation showing actin-filled plasma membrane protrusions, pearling/budding profiles,
585 shed vesicles and protein densities observed at certain sites of high membrane curvature in
586 budding profiles and shed vesicles. (d) Quantification of shedding. Top panel – abundance of
587 shed vesicles at control sites versus sites of damage (# vesicles per μm^2 tomogram X-Y cross-
588 sectional area); Bottom panel – abundance of budding profiles at control sites of regular
589 filopodia versus sites of damage (# buds per μm^2 tomogram X-Y cross-sectional area). Each
590 data point represents a tomogram. In both pairwise comparisons, the distributions for the
591 samples are significantly different from each other as shown by Kolmogorov-Smirnov test (KS
592 test). (e) Size distribution of shed vesicles and budding profiles at damage sites (# vesicles or
593 buds in each size range per μm^2 tomogram X-Y cross-sectional area) along with the mean \pm
594 s.d. values. Scale bars – (a – panel i) 50 μm , (a – panels ii-iv) 10 μm , and (b-c) 200 nm.

595 **Fig. 3: Similarities between filopodia and damage site protrusions.**

596 (a-b) CryoET and corresponding segmentation of (a) filopodia at undamaged sites and (b)
597 plasma membrane protrusions at damage sites. (c) Quantification of the abundance of regular
598 filopodia at control sites versus that of plasma membrane protrusions at damage sites (μm total
599 length of protrusions per μm^2 tomogram X-Y cross-sectional area). (d) Distribution of widths of
600 filopodia versus damage site protrusions (% in each size range) along with their mean \pm s.d.
601 values. (e) Quantification of internal vesicles in filopodia versus damage site protrusions (#
602 vesicles per μm of protrusion length). (f) Distribution of lengths of linear actin filaments in
603 filopodia versus damage site protrusions (% in each size range) along with their mean values.
604 (g) Imaging FusionRed-Pls1 in HeLa cells grown on glass (i) before and (ii) after damage. The
605 damage area (yellow circle) is 3 μm in diameter and the time points after damage are denoted in
606 minutes:seconds. In (c) and (e), each data point represents a tomogram and the distributions for
607 the pairs of samples being compared are not significantly different from each other (as shown
608 by KS tests). Scale bars – (a – panel i) 200 nm, (g) 10 μm , and 100 nm for all other panels.

609

610 **Fig. 4: Live-cell light microscopy and cryoET of damage sites in the presence of**
611 **Wiskostatin.**

612 (a) Light microscopy images of three different HeLa cells treated with wiskostatin on glass, (i, iii,
613 v) before and (ii, iv, vi) after damage – (left panels) bright-field, and (right panels) CHMP4B-
614 EGFP imaging. The damage areas are 3 μm in diameter. (b) CryoET of damage sites in
615 wiskostatin-treated cells showing several aberrant membranes, a few plasma membrane
616 protrusions and a few shed vesicles. (c) Quantification of plasma membrane protrusions at
617 damage sites (total length of protrusions in μm per μm^2 tomogram X-Y cross-sectional area) in
618 wiskostatin-treated cells versus untreated cells. (d) Size distribution of shed vesicles at damage
619 sites in wiskostatin-treated cells versus untreated cells (# vesicles in each size range per μm^2
620 tomogram X-Y cross-sectional area) along with mean \pm s.d. values. (e) Quantification of shed

621 vesicles at damage sites in wiskostatin-treated cells versus untreated cells (# vesicles per μm^2
622 tomogram X-Y cross-sectional area). In (c) and (e), each data point represents a tomogram and
623 the distributions for the pairs of samples being compared are significantly different from each
624 other as shown by KS tests. Scale bars – (a-b) 5 μm , and (c) 200 nm.

625

626 **Fig. 5: Live-cell light microscopy and cryoET of damage sites in Myo1a knockdown cells.**

627 (a) Light microscopy images of Myo1a knockdown HeLa cells grown on glass (i) before, and (ii-
628 v) at various time points after damage – (left panels) bright-field, and (right panels) CHMP4B-
629 EGFP imaging. The damage area is 3 μm in diameter. (b) CryoET of damage sites in Myo1a
630 knockdown cells showing actin-filled plasma membrane protrusions, pearling/budding profiles,
631 shed vesicles, protein densities observed at certain sites of high membrane curvature in
632 budding profiles and shed vesicles, defective budding profiles and long constriction necks. (c)
633 Width distribution of damage site protrusions in Myo1a knockdown cells versus wildtype (% in
634 each size range) along with mean \pm s.d. values. (d) Quantification of budding profiles at damage
635 sites of Myo1a knockdown cells versus wildtype (# buds per μm^2 tomogram X-Y cross-sectional
636 area). Each data point represents a tomogram. In (c) and (d), the distributions for the pairs of
637 samples being compared are significantly different from each other as shown by KS tests. Scale
638 bars – (a) 10 μm , and (b) 200 nm.

639

640 **Fig. 6: Live-cell light microscopy and cryoET of damage sites in Vps4B knockdown cells.**

641 (a) Light microscopy images of Vps4B knockdown HeLa cells grown on glass (i) before, and (ii-
642 v) at various time points after damage – (left panels) bright-field, and (right panels) CHMP4B-
643 EGFP imaging. The damage area is 3 μm in diameter. (b) – CryoET of damage sites of Vps4B
644 knockdown cells showing actin-filled plasma membrane protrusions, pearling/budding profiles,
645 shed vesicles, protein densities observed at certain sites of high membrane curvature in

646 budding profiles and shed vesicles, chains of budding profiles, shed membrane protrusions
647 devoid of F-actin and nested protrusions. Scale bars – (a) 10 μm , and (b) 200 nm.

648

649 **Fig. 7: Model for damage-induced plasma membrane shedding.**

650 (i-ii) Actin and membrane are redirected to the site of damage from other regions of the cell
651 (including neighboring filopodia), often resulting in the formation of membrane blebs. (iii)
652 Membrane blebs are withdrawn into the cell and reorganized into membrane protrusions using
653 F-actin. (iv) F-actin depolymerization could cause membrane deformation and pearling. Proteins
654 that sense or induce high negative membrane curvature could provide additional force
655 necessary for membrane deformation (especially for smaller vesicles). Myo1a is involved in
656 building protrusions and/or vesicle shedding while Vps4B is involved in membrane scission and
657 shedding, especially of smaller vesicles.

658

659 **Supplementary Material:**

660 **Supplementary Fig. 1: Live-cell light microscopy of plasma membrane damage site**
661 **showing pearling.**

662 Light microscopy images of HeLa cells grown on glass (i) before, and (ii-iv) at various time
663 points after damage showing membrane pearling – (left panels) bright-field images, (middle
664 panels) magnified images of insets in the left panels, and (right panels) CHMP4B-EGFP
665 images. The damage area is 3 μm in diameter. Scale bars – 10 μm .

666

667 **Supplementary Fig. 2: Live-cell light microscopy of plasma membrane damage site**
668 **showing retraction fibers.**

669 Light microscopy images of HeLa cells grown on glass (i) before, and (ii-iii) at various time
670 points after damage – (left panels) bright-field images showing retraction fibers, and (right

671 panels) CHMP4B-EGFP images showing its recruitment to the retraction fibers. The damage
672 area is 3 μm in diameter. Scale bars – 10 μm .

673

674 **Supplementary Fig. 3: Schematic for the experimental CLEM workflow.**

675

676 **Supplementary Fig. 4: Efficiency of siRNA transfection and Myo1a knockdown.**

677 (a) (i) Western blot showing the protein levels of Myo1a upon siRNA-mediated knockdown
678 compared to control siRNA transfected cells. Actin serves as the loading control. (ii)
679 Quantification of Myo1a protein levels from three different knockdown experiments relative to
680 control siRNA transfection experiments and normalized using actin loading control. s.d. values
681 are shown as error bars. (b) Light microscopy images of damaged cell in Fig. 5a – (left) bright-
682 field image, (middle) CHMP4B-EGFP expression, and (right) BLOCK-iT-AlexaFluor-Red control
683 RNA; the latter used as a readout for transfection efficiency.

684

685 **Supplementary Fig. 5: Damage response in Myo1a knockdown cells by cryoET.**

686 (a) Quantification of plasma membrane protrusions at damage sites of Myo1a knockdown cells
687 versus wildtype (total length of protrusions in μm / μm^2 tomogram X-Y cross-sectional area). (b)
688 Quantification of shed vesicles at damage sites of Myo1a knockdown cells versus wildtype (#
689 vesicles / μm^2 tomogram X-Y cross-sectional area). (c) Size distribution of shed vesicles at
690 damage sites of Myo1a knockdown cells versus wildtype (# vesicles in each size range / μm^2
691 tomogram X-Y cross-sectional area) along with their mean \pm s.d. values. (d) Size distribution of
692 budding profiles at damage sites of Myo1a knockdown cells versus wildtype (# budding profiles
693 in each size range / μm^2 tomogram X-Y cross-sectional area) along with their mean \pm s.d.
694 values. In (a) and (b), each data point represents a tomogram and the distributions for the pairs
695 of samples being compared are not significantly different from each other as shown by KS tests.

696

697 **Supplementary Fig. 6: Efficiency of siRNA transfection and Vps4B knockdown.**

698 (a) (i) Western blot showing a reduction in the protein levels of Vps4B upon siRNA-mediated
699 knockdown compared to control siRNA transfected cells. Actin serves as the loading control. (ii)
700 Quantification of Vps4B protein levels from three different knockdown experiments relative to
701 control siRNA transfection experiments and normalized using actin loading control. s.d. values
702 are shown as error bars. (b) Light microscopy images of damaged cell in Fig. 6a – (left) bright-
703 field image, (middle) CHMP4B-EGFP expression, and (right) BLOCK-iT-AlexaFluor-Red control
704 RNA; the latter used as a readout for transfection efficiency.

705

706 **Supplementary Fig. 7: Damage response in Vps4B knockdown cells by cryoET.**

707 (a) Quantification of plasma membrane protrusions at damage sites of Vps4B knockdown cells
708 versus wildtype (total length of protrusions in μm / μm^2 tomogram X-Y cross-sectional area).
709 Each data point represents a tomogram. The two distributions are significantly different from
710 each other as shown by KS test. However, their means are very similar (~ 2.5 μm of protrusions
711 per μm^2 tomogram X-Y cross-sectional area). (b) Size distribution of shed vesicles at damage
712 sites of Vps4B knockdown cells versus wildtype (# vesicles in each size range / μm^2 tomogram
713 X-Y cross-sectional area) along with their mean \pm s.d. values. (c) Size distribution of budding
714 profiles at damage sites of Vps4B knockdown cells versus wildtype (# buds in each size range /
715 μm^2 tomogram X-Y cross-sectional area) along with their mean \pm s.d. values. (d) Width
716 distribution of protrusions at damage sites of Vps4B knockdown cells versus wildtype (% in each
717 size range) along with their mean \pm s.d. values. In each of the pairwise comparisons, the
718 distributions for the two samples were significantly different from each other as indicated by the
719 p-values of KS tests.

720

721 **Supplementary Movie 1: Live-cell light microscopy of laser-damaged cells (6 cells,**
722 **including the one shown in Fig. 1).**

723

724 **Supplementary Movie 2: Representative experiment including CLEM, cryoET and**
725 **segmentation of a damage site.**

726

727 **Supplementary Movie 3: Live-cell light microscopy of a laser-damaged cell showing**
728 **FusionRed-Pls1 localization in both regular filopodia and damage-induced protrusions.**

729 The damage area (yellow circle) is 3 μm in diameter and the time points after damage are
730 denoted in minutes:seconds.

731 **References**

- 732 1. Babiychuk, E.B., Monastyrskaya, K., Potez, S. & Draeger, A. Intracellular Ca²⁺
733 operates a switch between repair and lysis of streptolysin O-perforated cells. *Cell*
734 *death and differentiation* **16**, 1126-1134 (2009).
- 735 2. Jimenez, A.J. *et al.* ESCRT machinery is required for plasma membrane repair.
736 *Science* **343**, 1247136 (2014).
- 737 3. Keefe, D. *et al.* Perforin triggers a plasma membrane-repair response that facilitates
738 CTL induction of apoptosis. *Immunity* **23**, 249-262 (2005).
- 739 4. Bi, G.Q., Alderton, J.M. & Steinhardt, R.A. Calcium-regulated exocytosis is required for
740 cell membrane resealing. *The Journal of cell biology* **131**, 1747-1758 (1995).
- 741 5. Miyake, K. & McNeil, P.L. Vesicle accumulation and exocytosis at sites of plasma
742 membrane disruption. *The Journal of cell biology* **131**, 1737-1745 (1995).
- 743 6. Reddy, A., Caler, E.V. & Andrews, N.W. Plasma membrane repair is mediated by
744 Ca²⁺-regulated exocytosis of lysosomes. *Cell* **106**, 157-169 (2001).
- 745 7. Andrews, N.W., Almeida, P.E. & Corrotte, M. Damage control: cellular mechanisms of
746 plasma membrane repair. *Trends in cell biology* **24**, 734-742 (2014).
- 747 8. Idone, V. *et al.* Repair of injured plasma membrane by rapid Ca²⁺-dependent
748 endocytosis. *The Journal of cell biology* **180**, 905-914 (2008).
- 749 9. Corrotte, M., Fernandes, M.C., Tam, C. & Andrews, N.W. Toxin pores endocytosed
750 during plasma membrane repair traffic into the lumen of MVBs for degradation.
751 *Traffic* **13**, 483-494 (2012).
- 752 10. Keyel, P.A. *et al.* Streptolysin O clearance through sequestration into blebs that bud
753 passively from the plasma membrane. *Journal of cell science* **124**, 2414-2423 (2011).
- 754 11. Potez, S. *et al.* Tailored protection against plasmalemmal injury by annexins with
755 different Ca²⁺ sensitivities. *The Journal of biological chemistry* **286**, 17982-17991
756 (2011).
- 757 12. Walev, I. *et al.* Delivery of proteins into living cells by reversible membrane
758 permeabilization with streptolysin-O. *Proceedings of the National Academy of*
759 *Sciences of the United States of America* **98**, 3185-3190 (2001).
- 760 13. Cocucci, E., Racchetti, G. & Meldolesi, J. Shedding microvesicles: artefacts no more.
761 *Trends in cell biology* **19**, 43-51 (2009).
- 762 14. Hooton, D., Lentle, R., Monro, J., Wickham, M. & Simpson, R. The Secretion and Action
763 of Brush Border Enzymes in the Mammalian Small Intestine. *Reviews of physiology,*
764 *biochemistry and pharmacology* **168**, 59-118 (2015).
- 765 15. Bates, J.M., Akerlund, J., Mittge, E. & Guillemin, K. Intestinal alkaline phosphatase
766 detoxifies lipopolysaccharide and prevents inflammation in zebrafish in response to
767 the gut microbiota. *Cell host & microbe* **2**, 371-382 (2007).
- 768 16. Shifrin, D.A., Jr. *et al.* Enterocyte microvillus-derived vesicles detoxify bacterial
769 products and regulate epithelial-microbial interactions. *Current biology : CB* **22**, 627-
770 631 (2012).
- 771 17. Distler, J.H. *et al.* Microparticles as regulators of inflammation: novel players of
772 cellular crosstalk in the rheumatic diseases. *Arthritis and rheumatism* **52**, 3337-3348
773 (2005).
- 774 18. Gasser, O. & Schifferli, J.A. Activated polymorphonuclear neutrophils disseminate
775 anti-inflammatory microparticles by ectocytosis. *Blood* **104**, 2543-2548 (2004).

- 776 19. MacKenzie, A. *et al.* Rapid secretion of interleukin-1beta by microvesicle shedding.
777 *Immunity* **15**, 825-835 (2001).
- 778 20. Proia, P. *et al.* Astrocytes shed extracellular vesicles that contain fibroblast growth
779 factor-2 and vascular endothelial growth factor. *International journal of molecular*
780 *medicine* **21**, 63-67 (2008).
- 781 21. Schiera, G. *et al.* Neurons produce FGF2 and VEGF and secrete them at least in part
782 by shedding extracellular vesicles. *Journal of cellular and molecular medicine* **11**,
783 1384-1394 (2007).
- 784 22. George, F.D. Microparticles in vascular diseases. *Thrombosis research* **122 Suppl 1**,
785 S55-59 (2008).
- 786 23. Janowska-Wieczorek, A. *et al.* Microvesicles derived from activated platelets induce
787 metastasis and angiogenesis in lung cancer. *International journal of cancer* **113**,
788 752-760 (2005).
- 789 24. Leroyer, A.S., Tedgui, A. & Boulanger, C.M. Role of microparticles in
790 atherothrombosis. *Journal of internal medicine* **263**, 528-537 (2008).
- 791 25. Crawley, S.W., Mooseker, M.S. & Tyska, M.J. Shaping the intestinal brush border. *The*
792 *Journal of cell biology* **207**, 441-451 (2014).
- 793 26. McConnell, R.E. & Tyska, M.J. Myosin-1a powers the sliding of apical membrane
794 along microvillar actin bundles. *The Journal of cell biology* **177**, 671-681 (2007).
- 795 27. Hsieh, C.W., Chu, C.H., Lee, H.M. & Yuan Yang, W. Triggering mitophagy with far-red
796 fluorescent photosensitizers. *Scientific reports* **5**, 10376 (2015).
- 797 28. Kochevar, I.E., Lambert, C.R., Lynch, M.C. & Tedesco, A.C. Comparison of
798 photosensitized plasma membrane damage caused by singlet oxygen and free
799 radicals. *Biochimica et biophysica acta* **1280**, 223-230 (1996).
- 800 29. Yang, W.Y. Optogenetic probing of mitochondrial damage responses. *Annals of the*
801 *New York Academy of Sciences* **1350**, 48-51 (2015).
- 802 30. Yang, J.Y. & Yang, W.Y. Bit-by-bit autophagic removal of parkin-labelled
803 mitochondria. *Nature communications* **4**, 2428 (2013).
- 804 31. Hung, Y.H., Chen, L.M., Yang, J.Y. & Yang, W.Y. Spatiotemporally controlled induction
805 of autophagy-mediated lysosome turnover. *Nature communications* **4**, 2111 (2013).
- 806 32. Bar-Ziv, R., Tlusty, T., Moses, E., Safran, S.A. & Bershadsky, A. Pearling in cells: a clue
807 to understanding cell shape. *Proceedings of the National Academy of Sciences of the*
808 *United States of America* **96**, 10140-10145 (1999).
- 809 33. Campelo, F. & Hernandez-Machado, A. Model for curvature-driven pearling
810 instability in membranes. *Physical review letters* **99**, 088101 (2007).
- 811 34. Charras, G.T., Hu, C.K., Coughlin, M. & Mitchison, T.J. Reassembly of contractile actin
812 cortex in cell blebs. *The Journal of cell biology* **175**, 477-490 (2006).
- 813 35. Kastner, B. *et al.* GraFix: sample preparation for single-particle electron
814 cryomicroscopy. *Nature methods* **5**, 53-55 (2008).
- 815 36. Shukla, A.K. *et al.* Visualization of arrestin recruitment by a G-protein-coupled
816 receptor. *Nature* **512**, 218-222 (2014).
- 817 37. Subramanian, P., Pirbadian, S., El-Naggar, M.Y. & Jensen, G.J. Ultrastructure of
818 *Shewanella oneidensis* MR-1 nanowires revealed by electron cryotomography.
819 *Proceedings of the National Academy of Sciences of the United States of America* **115**,
820 E3246-E3255 (2018).

- 821 38. Medalia, O. *et al.* Organization of actin networks in intact filopodia. *Current biology* :
822 *CB* **17**, 79-84 (2007).
- 823 39. Peterson, J.R. *et al.* Chemical inhibition of N-WASP by stabilization of a native
824 autoinhibited conformation. *Nature structural & molecular biology* **11**, 747-755
825 (2004).
- 826 40. Inoue, T., Pattabiraman, P.P., Epstein, D.L. & Vasantha Rao, P. Effects of chemical
827 inhibition of N-WASP, a critical regulator of actin polymerization on aqueous humor
828 outflow through the conventional pathway. *Experimental eye research* **90**, 360-367
829 (2010).
- 830 41. McConnell, R.E. *et al.* The enterocyte microvillus is a vesicle-generating organelle.
831 *The Journal of cell biology* **185**, 1285-1298 (2009).
- 832 42. Christ, L., Raiborg, C., Wenzel, E.M., Campsteijn, C. & Stenmark, H. Cellular Functions
833 and Molecular Mechanisms of the ESCRT Membrane-Scission Machinery. *Trends in*
834 *biochemical sciences* **42**, 42-56 (2017).
- 835 43. Hurley, J.H. ESCRTs are everywhere. *The EMBO journal* **34**, 2398-2407 (2015).
- 836 44. Garrus, J.E. *et al.* Tsg101 and the vacuolar protein sorting pathway are essential for
837 HIV-1 budding. *Cell* **107**, 55-65 (2001).
- 838 45. Pollet, H., Conrard, L., Cloos, A.S. & Tyteca, D. Plasma Membrane Lipid Domains as
839 Platforms for Vesicle Biogenesis and Shedding? *Biomolecules* **8** (2018).
- 840 46. Wood, W. *et al.* Wound healing recapitulates morphogenesis in *Drosophila* embryos.
841 *Nature cell biology* **4**, 907-912 (2002).
- 842 47. Casado, S., Lobo, M. & Paino, C.L. Dynamics of plasma membrane surface related to
843 the release of extracellular vesicles by mesenchymal stem cells in culture. *Scientific*
844 *reports* **7**, 6767 (2017).
- 845 48. Komaba, S. & Coluccio, L.M. Localization of myosin 1b to actin protrusions requires
846 phosphoinositide binding. *The Journal of biological chemistry* **285**, 27686-27693
847 (2010).
- 848 49. Masters, T.A. & Buss, F. Filopodia formation and endosome clustering induced by
849 mutant plus-end-directed myosin VI. *Proceedings of the National Academy of*
850 *Sciences of the United States of America* **114**, 1595-1600 (2017).
- 851 50. Heinrich, D., Ecke, M., Jasnin, M., Engel, U. & Gerisch, G. Reversible membrane
852 pearling in live cells upon destruction of the actin cortex. *Biophysical journal* **106**,
853 1079-1091 (2014).
- 854 51. Cauwenberghs, S. *et al.* Shedding of procoagulant microparticles from unstimulated
855 platelets by integrin-mediated destabilization of actin cytoskeleton. *FEBS letters*
856 **580**, 5313-5320 (2006).
- 857 52. Fox, J.E., Austin, C.D., Boyles, J.K. & Steffen, P.K. Role of the membrane skeleton in
858 preventing the shedding of procoagulant-rich microvesicles from the platelet
859 plasma membrane. *The Journal of cell biology* **111**, 483-493 (1990).
- 860 53. Middelhoven, P.J., van Buul, J.D., Kleijer, M., Roos, D. & Hordijk, P.L. Actin
861 polymerization induces shedding of FcγRIIIb (CD16) from human neutrophils.
862 *Biochemical and biophysical research communications* **255**, 568-574 (1999).
- 863 54. Mattila, P.K. & Lappalainen, P. Filopodia: molecular architecture and cellular
864 functions. *Nature reviews. Molecular cell biology* **9**, 446-454 (2008).
- 865 55. Zhao, H., Pykalainen, A. & Lappalainen, P. I-BAR domain proteins: linking actin and
866 plasma membrane dynamics. *Current opinion in cell biology* **23**, 14-21 (2011).

- 867 56. Mercenne, G., Alam, S.L., Ariei, J., Lalonde, M.S. & Sundquist, W.I. Angiotensin functions
868 in HIV-1 assembly and budding. *eLife* **4** (2015).
869 57. Iancu, C.V. *et al.* Electron cryotomography sample preparation using the Vitrobot.
870 *Nature protocols* **1**, 2813-2819 (2006).
871 58. Mastrorade, D.N. Automated electron microscope tomography using robust
872 prediction of specimen movements. *Journal of structural biology* **152**, 36-51 (2005).
873 59. Kremer, J.R., Mastrorade, D.N. & McIntosh, J.R. Computer visualization of three-
874 dimensional image data using IMOD. *Journal of structural biology* **116**, 71-76 (1996).
875 60. Agulleiro, J.I. & Fernandez, J.J. Fast tomographic reconstruction on multicore
876 computers. *Bioinformatics* **27**, 582-583 (2011).
877
878
879
880
881
882

Table 1 - Live-cell microscopy of cells after laser damage

Laser Damage	CHMP4B-EGFP recruitment	Blebbing	Retraction of blebs	Loss of filopodia	Appearance of at least 1 new protrusion	Partial retraction of cell area	Actin relocation
150 pulse cycles of laser damage							
Damaged	22/26	21/26	8/21	22/26	20/26	3/26	10/11
Control	0/25	0/25	-	4/25	17/25	0/25	0/2
100 pulse cycles of laser damage							
Damaged	18/22	11/22	5/11	13/22	6/22	3/22	4/7
Control	0/7	0/7	-	0/7	2/7	0/7	0/3
Total							
Damaged	40/48	32/48	13/32	35/48	26/48	6/48	14/18
Control	0/32	0/32	-	4/32	19/32	0/32	0/5

883

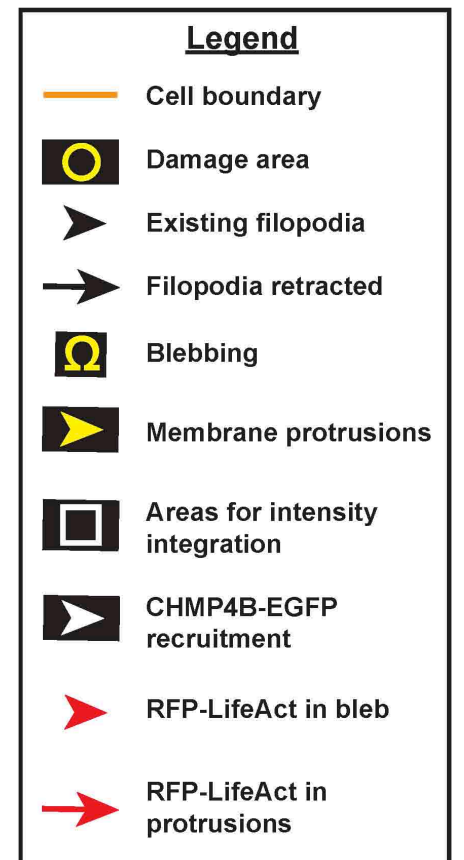
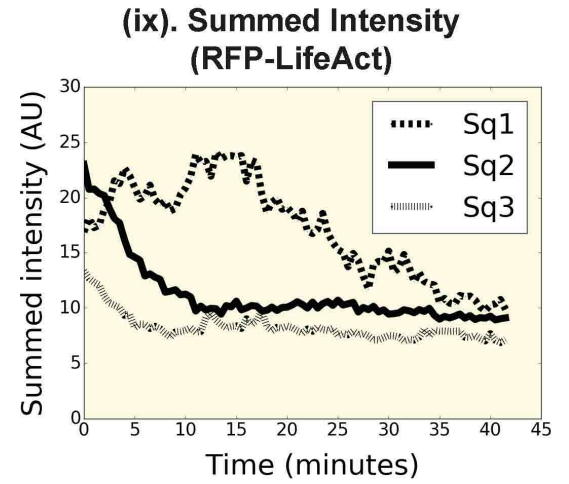
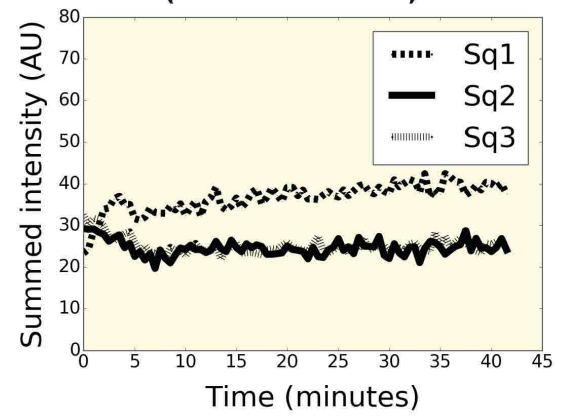
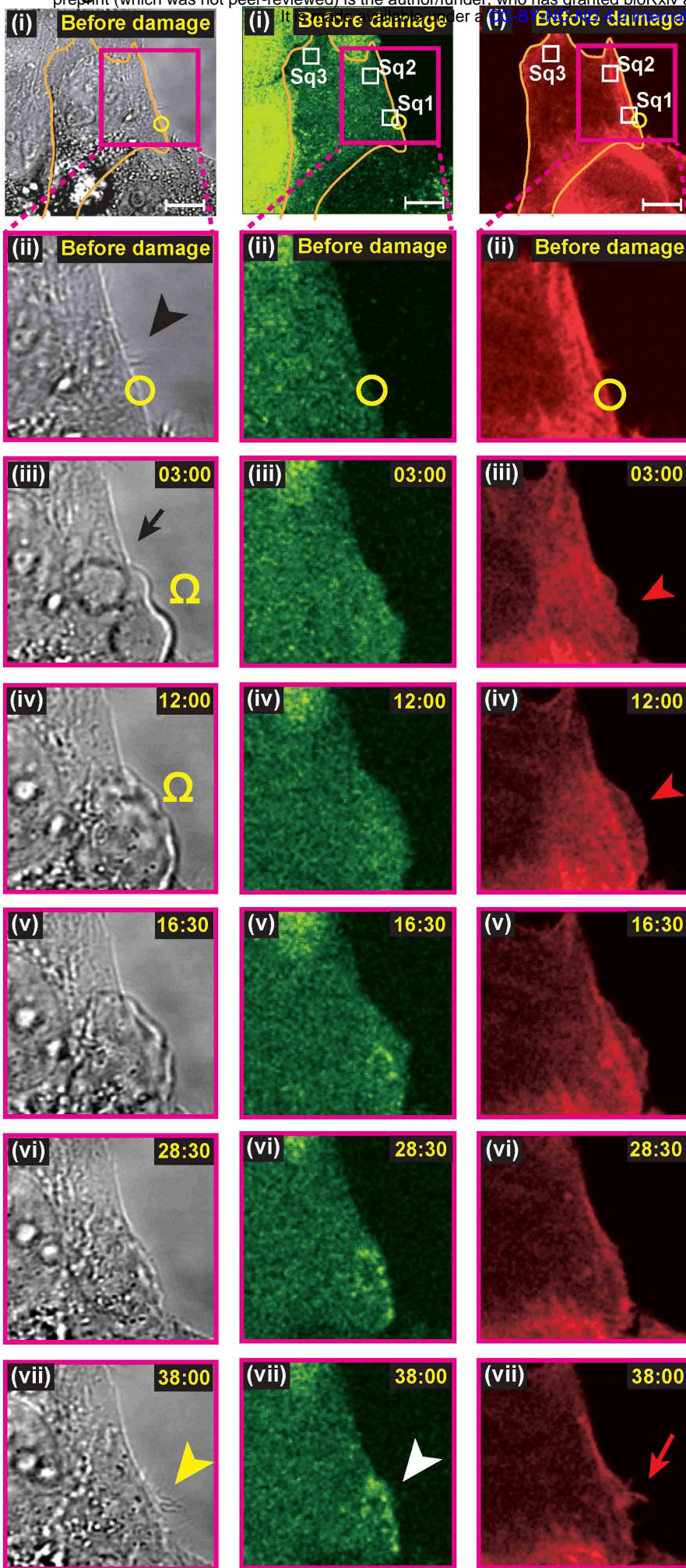


Fig. 1: Live-cell light microscopy of plasma membrane damage sites.

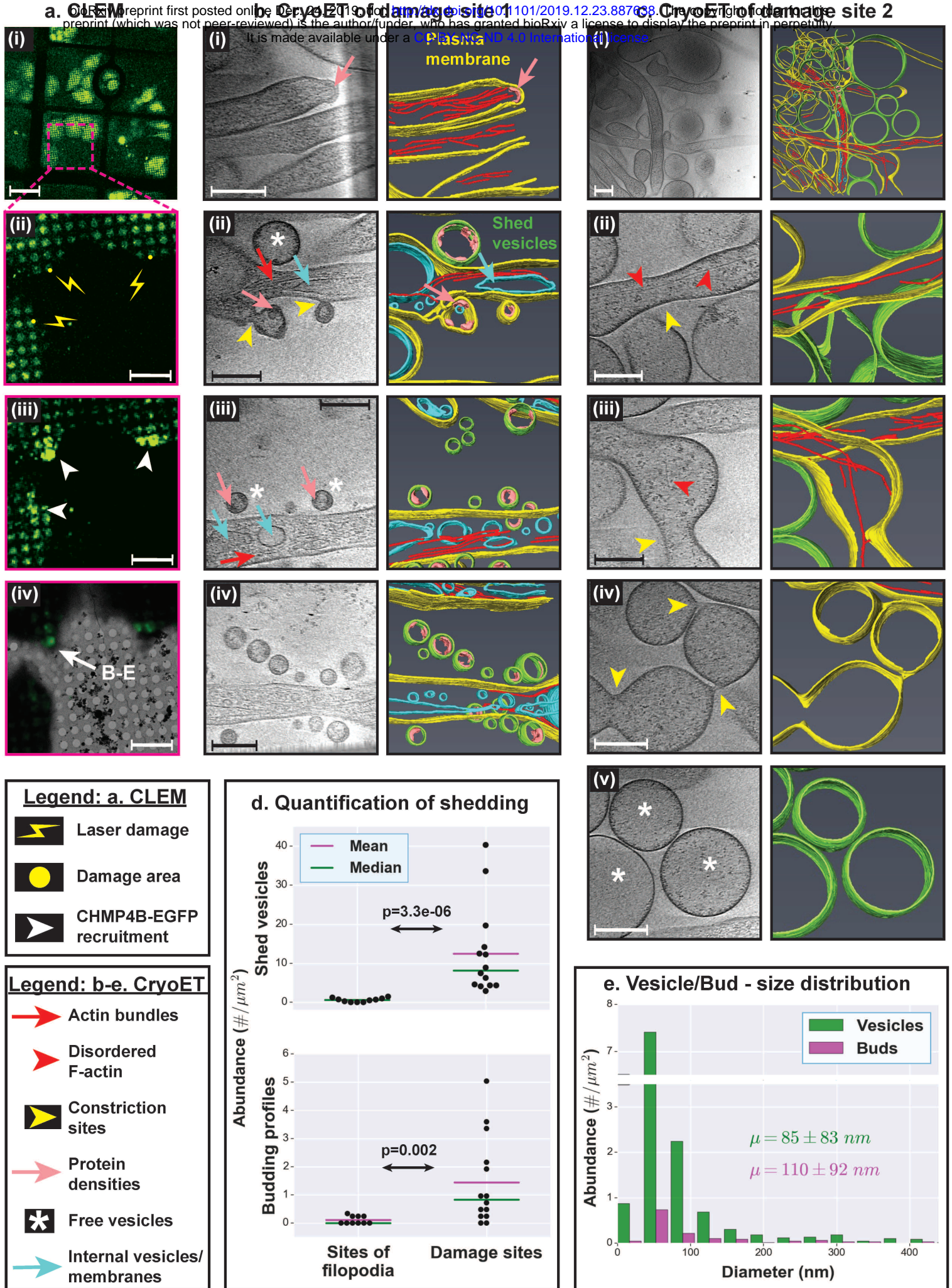


Fig. 2: CLEM and cryoET of plasma membrane damage sites.

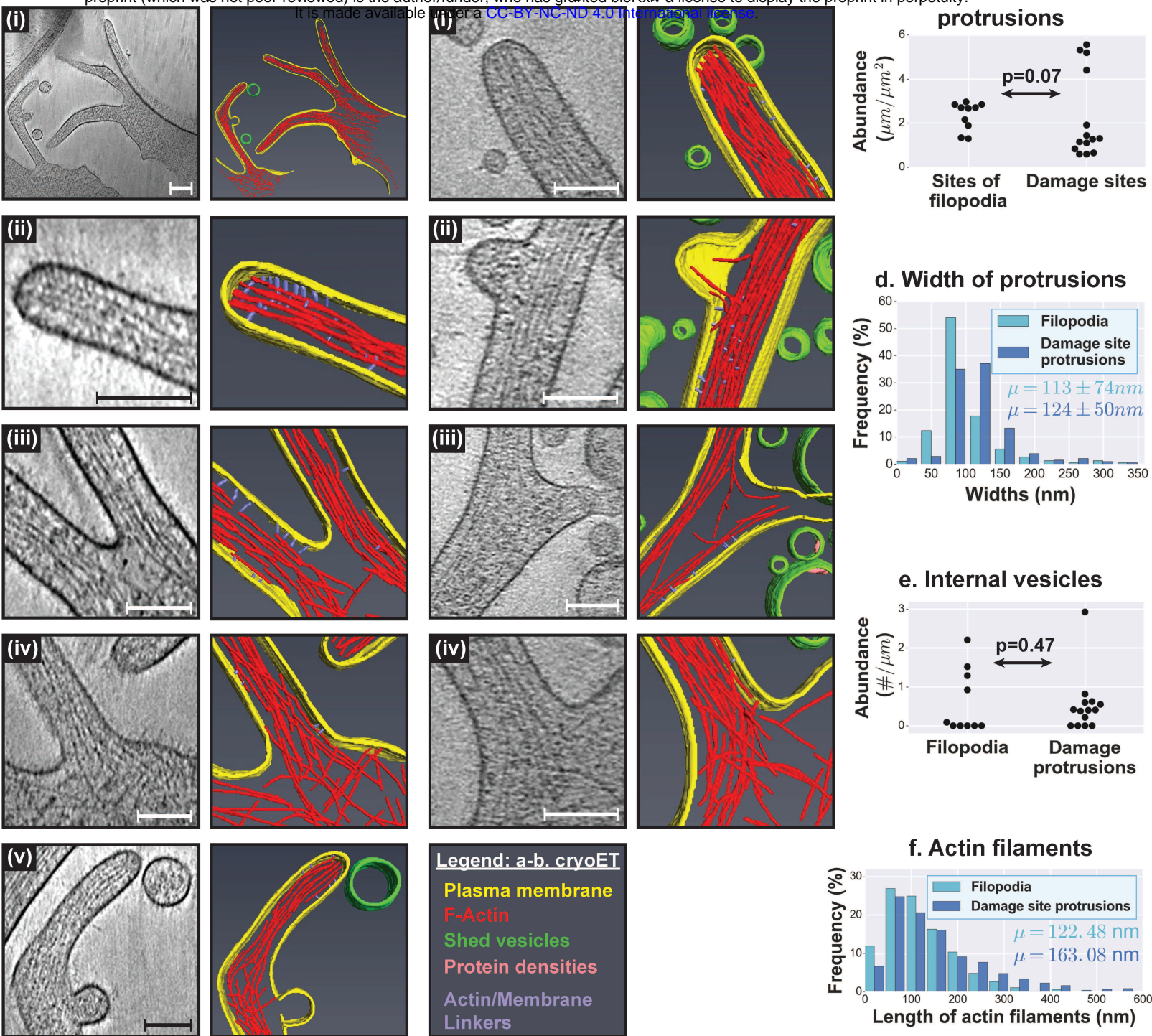
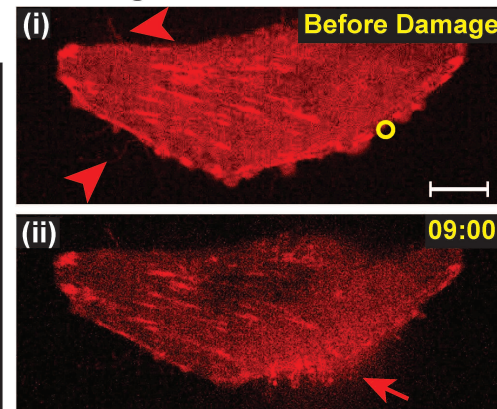


Fig. 3: Similarities between filopodia and damage site protrusions.

g. FusionRed-Pls1



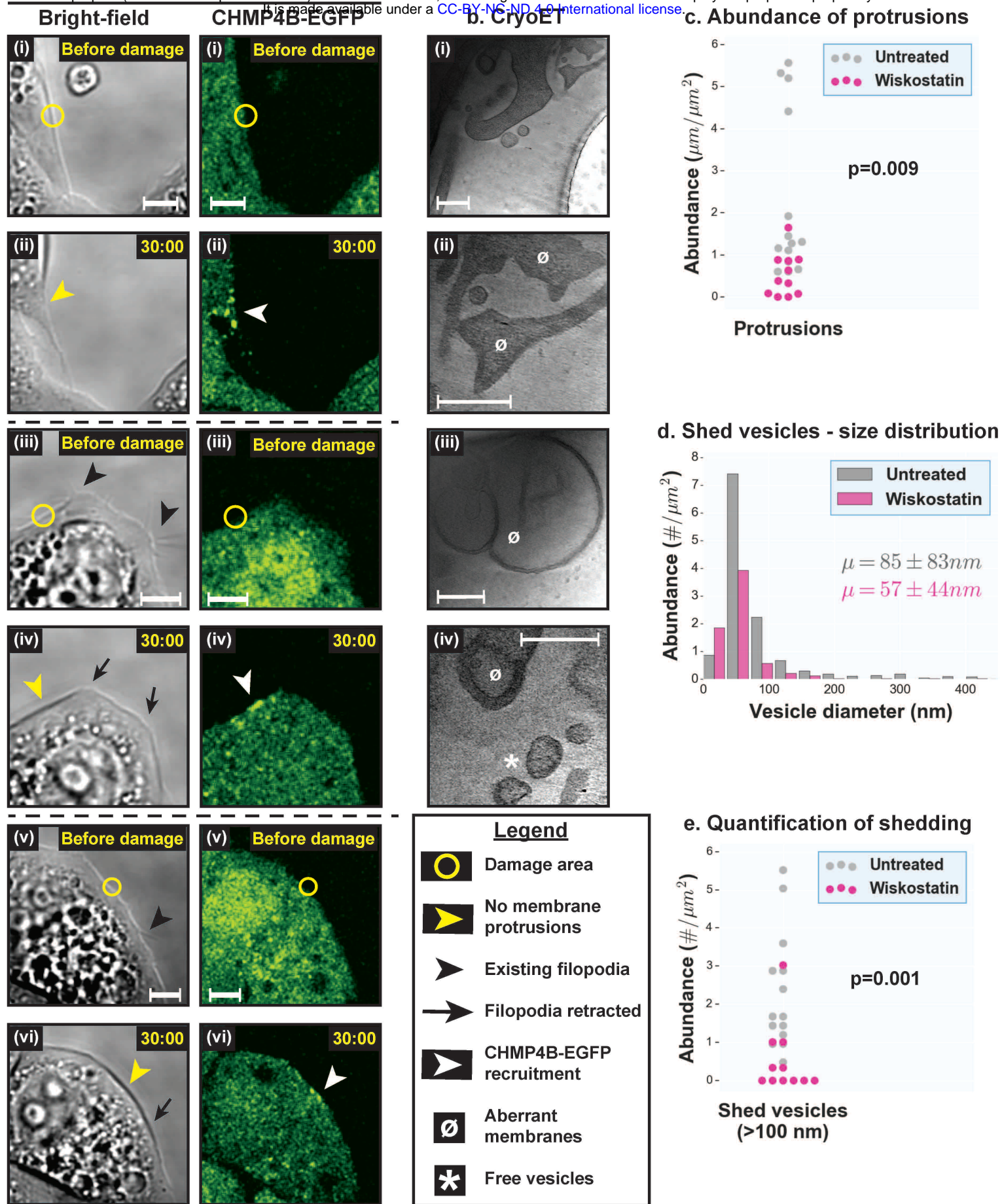


Fig. 4: Live-cell light microscopy and cryoET of damage sites in the presence of Wiskostatin.

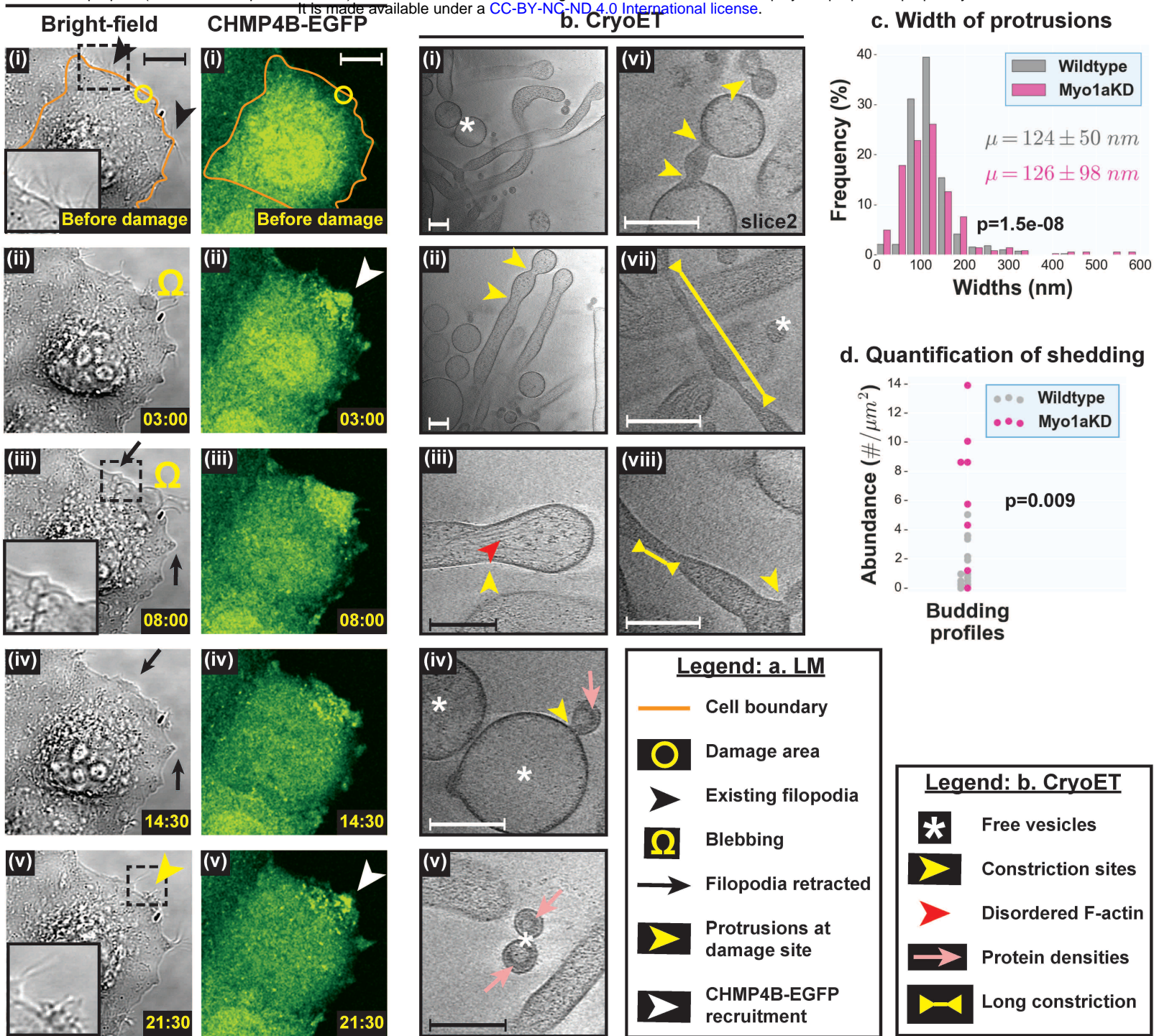


Fig. 5: Live-cell light microscopy and cryoET of damage sites in Myo1a knockdown cells.

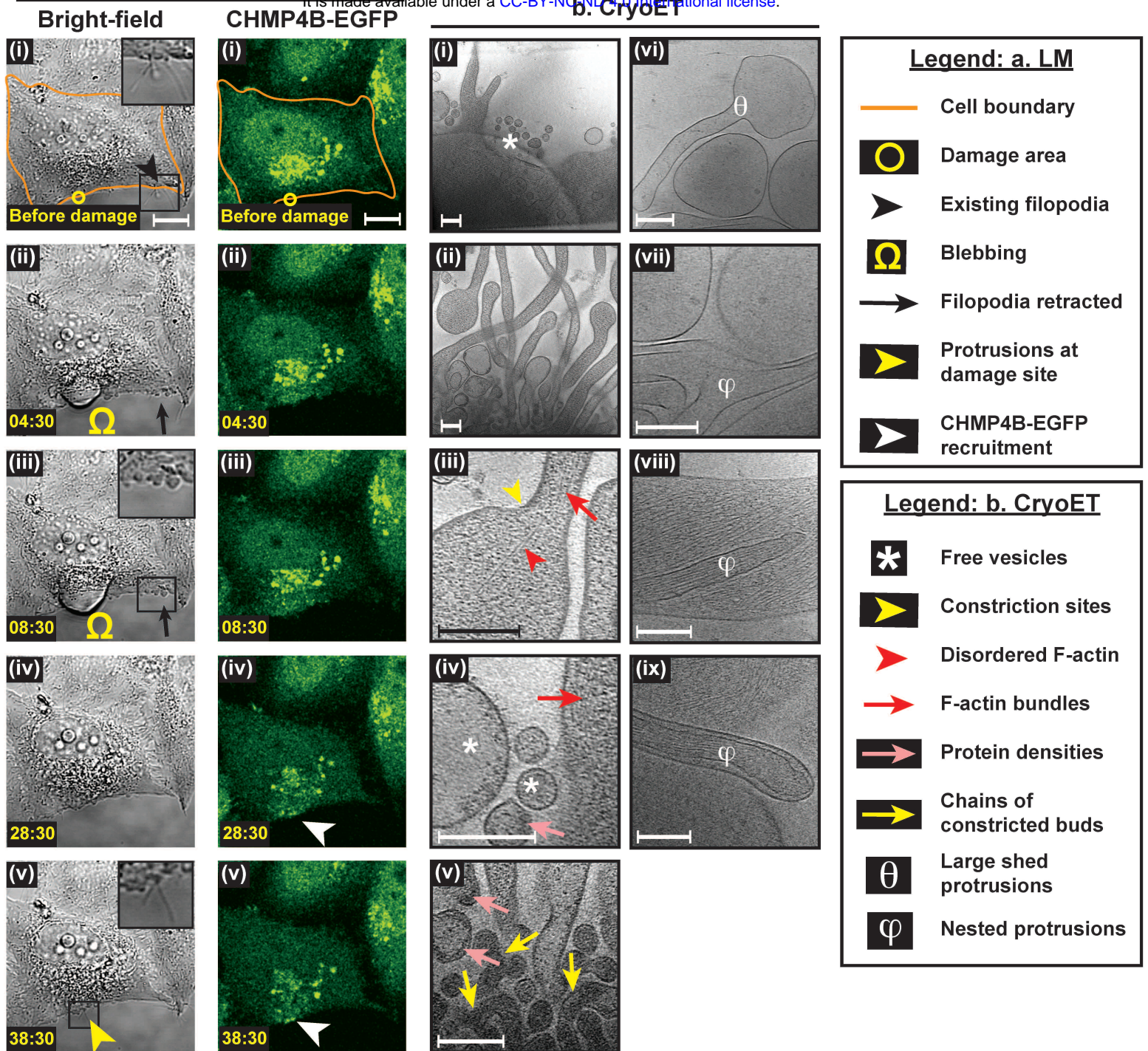


Fig. 6: Live-cell light microscopy and cryoET of damage sites in Vps4B knockdown cells.

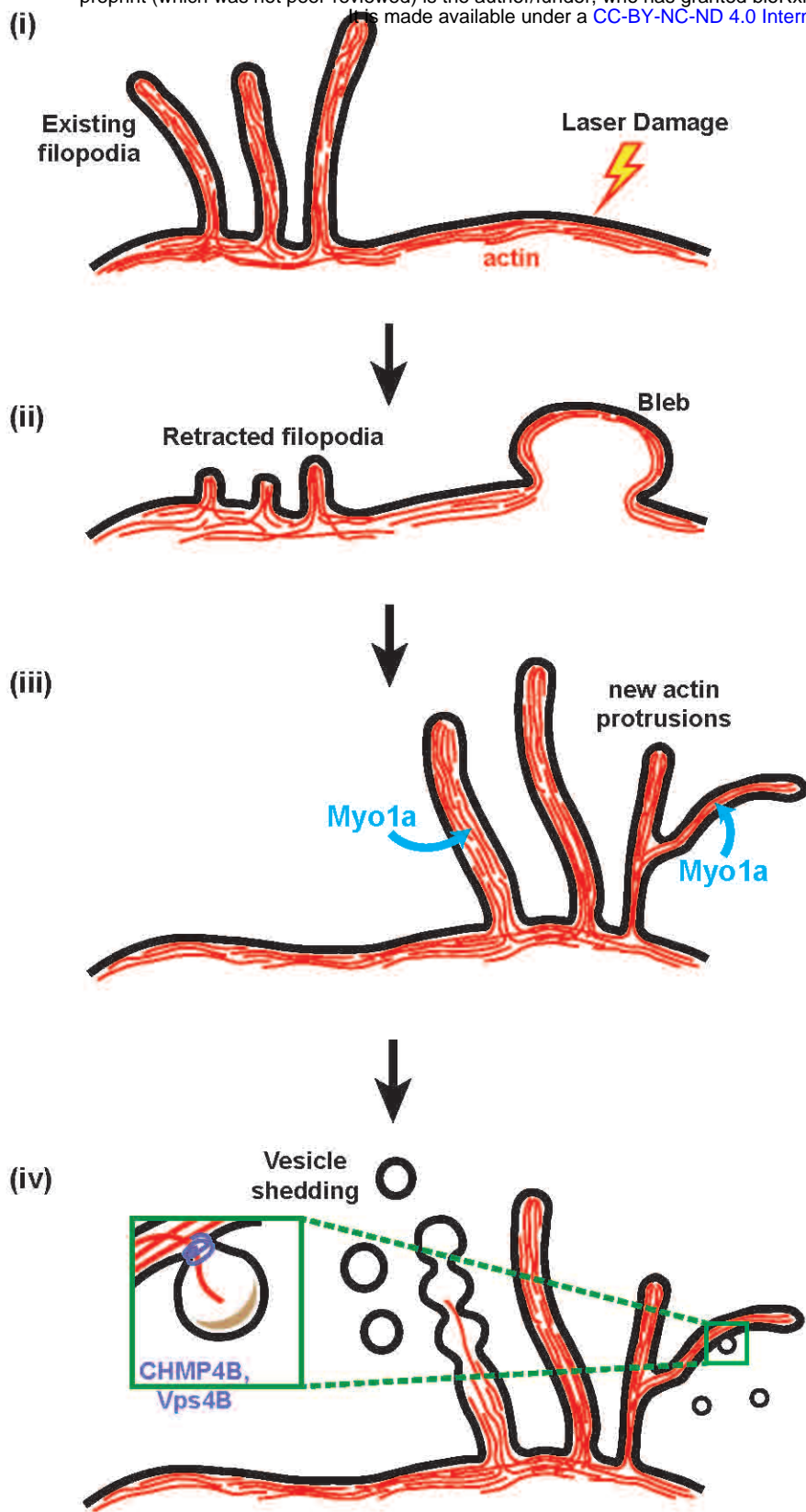


Fig. 7: Model for damage-induced plasma membrane shedding.